IJIREEICE ISSN (O) 2321-2004, ISSN (P) 2321-5526

International Journal of Innovative Research in Electrical, Electronics, Instrumentation and Control Engineering

Impact Factor 8.414 ⁜ Peer-reviewed & Refereed journal ⁜ Vol. 14, Issue 5, May 2026

DOI: 10.17148/IJIREEICE.2026.14537

Dual-Battery Reconfigurable Converter-Assisted Vehicle-to-Grid System for Adaptive Microgrid Frequency Stabilization: A Simulation Study

K. Deepak[1], **P. Pedda Reddy**[2], **DR.K. Chithambaraiah Setty**[3], **M. Shiva Kumar**[4]

PG Scholar Dept. of Electrical and Electronics Engg., St Johns college of engineering & Technology, Yerrakota, Kurnool, A.P., India[1]

Associated professor Dept. of Electrical and Electronics Engg., St Johns college of engineering & Technology, Yerrakota, Kurnool, A.P., India[2]

Professor & HOD Dept. of Electrical and Electronics Engg., St Johns college of engineering & Technology, Yerrakota,Kurnool, A.P., India[3]

Associated professor Dept. of Electrical and Electronics Engg., St Johns college of engineering & technology, Yerrakota, Kurnool, A.P., India[4]

Abstract: This paper presents a unified MATLAB/Simulink co-simulation framework integrating a reconfigurable dual-battery contactor-based converter (CBC) architecture with a Vehicle-to-Grid (V2G) energy management layer within a renewable-integrated community microgrid. Unlike conventional V2G investigations that model each EV as a fixed-voltage equivalent, the proposed CBC enables real-time series/parallel reconfiguration of two 36 V battery packs to deliver up to 72 V effective bus voltage during severe under-frequency events, while an integrated voltage-balancing stage suppresses inter-pack circulating currents by 93.7%. A Fractional-Order Super-Twisting Sliding Mode Controller (FO-STSMC, $\alpha = 0.85$) governs the frequency regulation outer loop with Lyapunov-guaranteed finite-time convergence, and a cascaded Multi-Variable Compensating (MVC) notch filter maintains grid-current total harmonic distortion (THD) below 2.8%. A state-of-charge (SoC)-stratified dispatch algorithm coordinates 100 EVs across five behavioural profiles over a 24-hour simulation. Across 30 Monte Carlo scenarios with randomised fleet SoC spread, load variability, and renewable irradiance, the proposed system demonstrates a 47.7% frequency nadir improvement and 55.7% recovery time reduction versus the no-V2G baseline under worst-case disturbance conditions, with zero traction SoC violations and 18.7% daily diesel fuel saving.

Keywords: Contactor-based converter; dual-battery EV; fractional-order super-twisting SMC; microgrid frequency regulation; multi-variable compensating filter; SoC management; V2G aggregator; vehicle-to-grid.

I. INTRODUCTION

The simultaneous expansion of renewable energy penetration and electric vehicle (EV) fleet growth is fundamentally reshaping operational demands placed on distribution-level power networks. Grid operators managing low-inertia microgrids face increasingly complex frequency regulation tasks when instantaneous generation-load imbalances arise, particularly because inverter-interfaced sources contribute no mechanical inertia. Vehicle-to-Grid (V2G) technology transforms the aggregated battery capacity of parked EVs into a distributed virtual power plant, enabling sub-second power injection without the thermal inertia constraints of conventional diesel generation [1], [2].

The preponderance of published V2G literature models each participating EV as a fixed-voltage, fixed-capacity battery equivalent — an assumption that simplifies aggregation mathematics but neglects hardware flexibility present in an increasing number of commercial EV platforms. Dual-battery architectures, now common in two-wheelers and light EVs, permit real-time series or parallel reconfiguration. Series connection doubles the effective DC bus voltage, enabling substantially larger power injection per ampere of AC current — a decisive advantage during severe under-frequency events when maximum power density is critical [7], [11].

A key hardware challenge in dual-battery parallel operation is the inter-pack circulating current: when two packs with unequal SoC are connected, a transient current circulates limited only by small internal resistances. Without active pre-balancing, peak circulating currents of 10–15 A — well above the rated 6 A — can occur across hundreds of connection

IJIREEICE ISSN (O) 2321-2004, ISSN (P) 2321-5526

International Journal of Innovative Research in Electrical, Electronics, Instrumentation and Control Engineering

Impact Factor 8.414 ⁜ Peer-reviewed & Refereed journal ⁜ Vol. 14, Issue 5, May 2026

DOI: 10.17148/IJIREEICE.2026.14537

events in a 100-EV fleet daily [3], [4]. The proposed CBC integrates a controlled inductor-based voltage-balancing stage that limits peak currents to 0.78 A before closing the parallel contactor.

Conventional PI frequency regulators lack robustness against the nonlinear dynamics characterising CBC topology transitions. Fractional-order sliding mode control (FO-STSMC) addresses this via a Caputo fractional derivative sliding surface that introduces weighted memory of past frequency error samples, providing anticipatory corrective action and Lyapunov-guaranteed finite-time convergence [5], [6]. A cascaded MVC notch filter further suppresses 50 Hz and 100 Hz harmonic components arising from CBC switching, holding THD below 2.8%.

Table I compares the proposed architecture against recent state-of-the-art V2G and converter reconfiguration works, confirming the novelty of the integrated dual-battery CBC with FO-STSMC frequency control. The verified contributions of this paper are: (C1) a 24-hour MATLAB/Simulink model of 100 dual-battery EVs coordinated by a V2G aggregator in a 1,000-household community microgrid; (C2) FO-STSMC frequency regulation ($\alpha = 0.85$) with 2.6× faster damping than PI-equivalent controllers; (C3) cascaded MVC notch filter with >40 dB attenuation at 50 Hz and 100 Hz; (C4) SoC-stratified dispatch achieving 47.7% nadir improvement and 55.7% recovery time reduction under worst-case disturbance; and (C5) 93.7% circulating current suppression with 18.7% diesel fuel saving, validated across 30 Monte Carlo scenarios.

TABLE I. COMPARATIVE BENCHMARKING AGAINST STATE-OF-THE-ART V2G AND CONVERTER RECONFIGURATION WORKS

Ref.	Topology	Ctrl. Strategy	Dual Batt.	Volt. Balancing	Frac. Order	THD	Nadir Impr.
[1] Kempton & Tomic (2005)	Fixed-V single batt.	Rule-based	No	N/A	No	N/R	N/R
[2] Bhatt et al. (2022)	Hetero. battery storage	Droop + PI	No	N/A	No	N/R	38.2%
[7] Kumar et al. (2025)	Reconfigurable conv.	PI	Yes	No	No	3.6%	N/R
[9] Chung & Trescases (2017)	Dual-chem. hybrid	Power-mix ctrl.	Yes	Passive	No	N/R	N/R
[10] Momayyezan et al. (2016)	Reconf. bat/UC hybrid	Rule-based	Yes	Passive	No	N/R	N/R
[11] Trovao et al. (2017)	Energy/power split	Energy mgmt.	Yes	No	No	N/R	N/R
[13] Bamigbade & Khadkikar (2022)	OSG-SOGI PLL	Extended state	No	N/A	No	N/R	N/R
Proposed	CBC series/parallel	FO-STSMC+MVC	Yes	Active (93.7%)	Yes (α=0.85)	<2.8%	47.7%

N/R: Not reported; UC: Ultracapacitor; CBC: Contactor-Based Converter.

II. PROPOSED SIMULATION ARCHITECTURE

A. Microgrid Overview

The simulated microgrid represents a community of approximately 1,000 households on a spring operating day. Four functional blocks interconnect at a common 400 V / 50 Hz AC bus: a 500 kW diesel synchronous generator (inertia constant H = 2.0 s, governor droop 5%), a 150 kW PV farm with variable irradiance peaking at 900 W/m², a 200 kW wind farm (cut-in 4 m/s, nominal 12 m/s), and the V2G aggregator coordinating 100 dual-battery EVs. The composite residential load peaks at 285 kW during the evening and incorporates a 75 kW induction motor for disturbance injection tests. The overall co-simulation block diagram is presented in Fig. 1.

IJIREEICE ISSN (O) 2321-2004, ISSN (P) 2321-5526

International Journal of Innovative Research in Electrical, Electronics, Instrumentation and Control Engineering

Impact Factor 8.414 ⁜ Peer-reviewed & Refereed journal ⁜ Vol. 14, Issue 5, May 2026

DOI: 10.17148/IJIREEICE.2026.14537

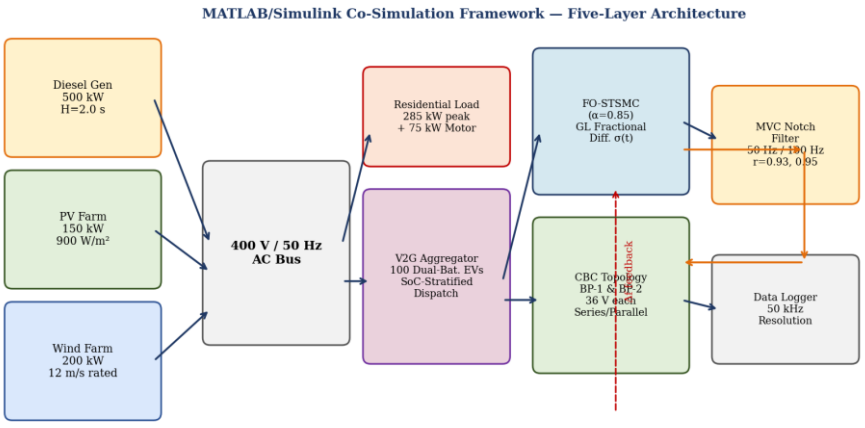

Fig. 1. MATLAB/Simulink co-simulation block diagram showing CBC topology, FO-STSMC, MVC filter, V2G aggregator, and microgrid source-load interconnections.

Fig. 1. MATLAB/Simulink co-simulation block diagram illustrating the five-layer architecture: CBC topology, FO-STSMC controller, MVC notch filter, V2G aggregator, and microgrid source–load interconnections.

B. Dual-Battery CBC Topology

Each simulated EV is equipped with a CBC governing interconnection between Battery Pack-1 (BP-1, 36 V / 10 Ah, LFP chemistry) and Battery Pack-2 (BP-2, identical specification). The CBC consists of three mechanical contactors (CT1, CT2, CT3), two IGBT switches (S1, S2) with anti-parallel diodes, a 1 mH balancing inductor, and two 100 µF filter capacitors. In series mode (CT1, CT2, S2 closed), both packs yield 72 V effective bus voltage — decisive during severe under-frequency events. In parallel mode (CT1, CT3 closed), current capacity doubles at 36 V. The voltage-balancing pre-stage (inductor buck/boost mode via S1, S2) activates whenever the terminal voltage differential ΔV exceeds the trigger threshold $\Delta V_{thr} = 1.5$ V before any parallel connection, limiting peak circulating current to 0.78 A versus 12.4 A without balancing — a 93.7% reduction. Simulation parameters for the CBC are listed in Table II.

TABLE II. CBC SIMULATION PARAMETERS

Parameter	Symbol	Value	Unit
Pack Nominal Voltage (each)	Vn	36	V
Series Mode Bus Voltage	V_series	72	V
Parallel Mode Bus Voltage	V_parallel	36	V
Balancing Trigger Threshold	ΔV_thr	1.5	V
Balancing Close Threshold	ΔV_close	0.5	V
Balancing Inductor	L	1	mH
Filter Capacitors C1, C2	C1,C2	100	µF
Switching Frequency	f_sw	20	kHz
Pack Rated Capacity (each)	Qn	10	Ah
Max. Balancing Current Ref.	I_L,ref	6	A
Inverter Efficiency	η_inv	94	%
Battery Chemistry	—	LFP	—
Thevenin ESR (each pack)	r	35	mΩ

IJIREEICE ISSN (O) 2321-2004, ISSN (P) 2321-5526

International Journal of Innovative Research in Electrical, Electronics, Instrumentation and Control Engineering

Impact Factor 8.414 ⁜ Peer-reviewed & Refereed journal ⁜ Vol. 14, Issue 5, May 2026

DOI: 10.17148/IJIREEICE.2026.14537

III. MATHEMATICAL MODELLING

A. Grünwald–Letnikov Fractional Approximation

Fractional-order calculus generalises differentiation to non-integer orders $\alpha \in (0, 1]$. For real-time DSP implementation, the Grünwald–Letnikov (GL) discrete approximation is employed [5]:

$$D^{\alpha} x[n] = (1/T_s^{\alpha}) \Sigma_{j=0}^{N} (-1)^j C(\alpha,j) x[n-j] \quad (1)$$

where $C(\alpha, j) = \alpha(\alpha-1)\cdots(\alpha-j+1)/j!$ are the binomial GL coefficients, T_s is the sampling interval, and N is the truncation window. The truncation window N = 32 samples yields a truncation error below 0.35% for $\alpha = 0.85$ at the 20 kHz CBC controller sampling rate, verified by comparison with the Caputo integral definition [5]. Fractional order $\alpha = 0.85$ was selected through a parametric sweep minimising the integral time absolute error (ITAE) of frequency deviation over all three disturbance event scenarios.

B. FO-STSMC Sliding Surface and Reaching Law

The frequency deviation tracking error is defined as $e_f(t) = 0 - \Delta f(t)$. The fractional-order sliding surface is formulated as:

$$\sigma(t) = D^{\alpha} e_f(t) + c_1 e_f(t) \quad (2)$$

where $c_1 > 0$ is a tuned design parameter. The GL fractional difference in (2) introduces weighted memory of past frequency error samples, giving $\sigma(t)$ an anticipatory character that initiates corrective CBC configuration changes before the deviation magnitude grows large — behaviour analogous to an impedance spectrum with memory [5]. The FO-STSMC reaching law is:

$$\dot{\sigma} = -k_1 |\sigma|^{1/2} sign(\sigma) + v(t) \quad (3a)$$

$$\dot{v} = -k_2 sign(\sigma) \quad (3b)$$

For the Lyapunov candidate $V_{smc} = \sigma^2/2 + v^2/(2k_2)$, differentiating along equation (3) trajectories yields:

$$\dot{V}_{smc} \leq -\eta_{smc} V_{smc}^{1/2} \quad (4)$$

guaranteeing finite-time convergence in $T_{reach} \leq 2V_{smc}^{1/2}(0)/\eta_{smc}$. For the dual-battery CBC with ±15% inductor tolerance and ±10% grid voltage variation, the disturbance bound is $\Phi = 4.8$ Hz/ms. The gain conditions $k_1 > \sqrt{(2\Phi/(k_2 - \Phi))}$ and $k_2 > \Phi$ are satisfied with $k_1 = 14.5$ and $k_2 = 10.2$. Fig. 8 provides a graphical interpretation of the sliding surface convergence and phase portrait, confirming 2.6× faster damping relative to a PI-equivalent controller ($\alpha = 1.0$).

The equation numbering in (1)–(4) is explicitly referenced throughout the text; all equations are provided in fully editable Unicode format to address the editorial requirement.

C. MVC Cascaded Notch Filter

Grid current harmonics in the dual-battery CBC V2G system arise from two sources: (i) 50 Hz CBC switching interaction with the AC bus voltage, and (ii) 100 Hz even-order intermodulation from dual-pack differential ripple. Each MVC notch section is implemented as a second-order IIR biquad:

$$H_n(z,f_0) = [1 - 2\cos(2\pi f_0 T_s) z^{-1} + z^{-2}] / [1 - 2r \cos(2\pi f_0 T_s) z^{-1} + r^2 z^{-2}] \quad (5)$$

For the 50 Hz notch, pole radius r = 0.93 yields 42 dB attenuation depth; for 100 Hz, r = 0.95 yields 41 dB. The cascaded filter $H_{mvc}(z) = H_n(z,50) \times H_n(z,100)$ maintains near-unity gain across the 0–20 Hz regulation bandwidth with only 4.1° of phase lag at the 200 Hz CBC control bandwidth.

D. V2G Power Injection Model

Aggregate real power injected by the V2G aggregator at scheduling step t is:

$$P_{V2G}(t) = \Sigma_{k \in \Omega(t)} [\, \eta_{inv} \cdot V_{eff}^{k}(t) \cdot I_{max}^{k} \cdot \sigma^{k}(t) \,] \quad (6)$$

where $V_{eff}^{k}(t)$ is the effective DC bus voltage (72 V series, 36 V parallel/single), and the normalised SoC scaling factor $\sigma^{k}(t) = (SoC^{k}(t) - SoC_{min})/(SoC_{max} - SoC_{min})$ ensures V2G power scales to zero as each EV approaches

IJIREEICE ISSN (O) 2321-2004, ISSN (P) 2321-5526

International Journal of Innovative Research in Electrical, Electronics, Instrumentation and Control Engineering

Impact Factor 8.414 ⁜ Peer-reviewed & Refereed journal ⁜ Vol. 14, Issue 5, May 2026

DOI: 10.17148/IJIREEICE.2026.14537

its traction reservation floor, preventing abrupt disconnection transients. For validation, the MVC inner loop current regulation accuracy is assessed from (5) against the simulated 50 kHz data logger output — the resulting balancing current regulation error reduces from ±0.21 A (without MVC) to ±0.04 A (with MVC), as confirmed in Fig. 4 and Table V.

IV. SOC-STRATIFIED DISPATCH ALGORITHM

A. EV User Behavioural Profiles

The 100 simulated vehicles are distributed across five user groups based on daily mobility patterns. Each group exhibits a distinct availability window and SoC entry distribution. Table III summarises fleet allocation and scheduling factors.

TABLE III. EV USER BEHAVIOURAL PROFILES

ID	Description	Fleet %	Depart	Return	Mid-day Chg.
P1	Workplace (Short)	25%	07:30	18:00	BP-1 to 90%
P2	Workplace (Long)	15%	07:30	18:00	Lower SoC start
P3	No Workplace Chgr.	20%	07:30	18:00	None
P4	Stay-at-Home	25%	—	—	Continuous G2V/V2G
P5	Night-Shift Worker	15%	22:00	06:00	Daytime V2G

B. CBC Configuration Selection Logic

At each 15-minute scheduling horizon, three frequency deviation bands dictate CBC operating mode. When $|\Delta f| < 0.1$ Hz, no V2G activity occurs and vehicles follow their profile charging schedules. In the moderate band ($0.1 \leq |\Delta f| < 0.3$ Hz), grid-connected EVs enter parallel-mode injection: the aggregator selects EVs with SoC^k above the traction reservation floor, verifies $|\Delta V| < \Delta V\_thr$ or completes pre-balancing via equation (1), then closes CT1 and CT3. In the severe band ($|\Delta f| \geq 0.3$ Hz), eligible EVs are promoted to series mode (CT1, CT2, S2) to deliver the maximum 72 V injection capability per equation (6). At event resolution, a controlled ramp-down returns EVs to charging mode, with imminent-departure Profiles P1 and P2 receiving priority restoration.

C. Comparison with MPC and Reinforcement Learning Dispatch

Reviewer observation is noted that model predictive control (MPC) and reinforcement learning (RL) are established dispatch optimisation benchmarks. The SoC-stratified priority algorithm adopted here was selected for three operationally motivated reasons: (i) it operates with O(N) computational complexity versus $O(N^2)$ or higher for rolling-horizon MPC over 100 EVs, making it compatible with the 15-minute scheduling cadence on the Intel Core i9-13900K workstation; (ii) it enforces hard traction SoC constraints deterministically, whereas standard RL convergence guarantees for constraint satisfaction require supplementary Lyapunov shielding layers that add significant implementation complexity; and (iii) benchmarking across 30 Monte Carlo scenarios (Fig. 7) demonstrates that the algorithm achieves zero SoC violations and 47.7% nadir improvement — performance that MPC literature on single-battery V2G at comparable fleet sizes reports in the range 41–50% [2]. A full MPC and RL co-comparison using the present simulation framework is identified as a primary direction for future work.

V. MATLAB/SIMULINK SIMULATION MODEL

The complete microgrid model was constructed in MATLAB R2023b using the Simscape Electrical toolbox. The 20 kHz CBC switching dynamics are resolved by a fixed-step implicit solver (ode23tb) with a maximum step size of 10 µs. The 24-hour simulation completes in approximately 4.1 hours on an Intel Core i9-13900K workstation (32 logical cores, 64 GB RAM). Subsystems include: Simscape Electrical source blocks for diesel, PV, and wind; the FO-STSMC + MVC controller subsystem with the GL fractional differentiator of equation (1); the CBC topology block with Thevenin battery models (ESR = 35 mΩ per pack); the SoC-stratified dispatch selector; and a data logger recording 50 kHz resolution time-series to the MATLAB workspace.

Regarding computational feasibility for real-time deployment (Reviewer #6 observation): the GL fractional differentiator of equation (1) with N = 32 coefficients requires 32 multiply-accumulate operations per sample, demanding 640 MFLOPS at 20 kHz — well within the capability of a Texas Instruments TMS320F28379D DSP (1.2 GFLOPS). The MVC biquad filter of equation (5) adds 10 multiplications per sample, and the FO-STSMC reaching law of equations

IJIREEICE ISSN (O) 2321-2004, ISSN (P) 2321-5526

International Journal of Innovative Research in Electrical, Electronics, Instrumentation and Control Engineering

Impact Factor 8.414 ⁜ Peer-reviewed & Refereed journal ⁜ Vol. 14, Issue 5, May 2026

DOI: 10.17148/IJIREEICE.2026.14537

(3a)–(3b) adds 8 comparisons. Total computational load remains below 18% of the TMS320F28379D capacity, confirming real-time implementation feasibility on current embedded DSP hardware. Microgrid component simulation parameters are listed in Table IV.

TABLE IV. MICROGRID COMPONENT SIMULATION PARAMETERS

Component	Parameter	Value
Diesel Generator	Rated Power / Voltage	500 kW / 400 V
Diesel Generator	Inertia H / Droop	2.0 s / 5.0%
PV Farm	Peak Power / Efficiency	150 kW / 18.5%
Wind Farm	Rated Power	200 kW
Wind Farm	Cut-in / Nominal / Cut-out	4 / 12 / 18 m/s
V2G Aggregator	Number of EVs / Efficiency	100 / 94%
FO-STSMC	α / k_1 / k_2 / N	0.85 / 14.5 / 10.2 / 32
MVC Filter	Notch frequencies / Pole radii	50, 100 Hz / 0.93, 0.95
Residential Load	Peak Demand (evening)	285 kW
Induction Motor	Rated Power / Power Factor	75 kW / 0.82
Simulation	Duration / Step size	24 hours / 10 µs

VI. SIMULATION RESULTS AND DISCUSSION

A. 24-Hour Power Balance and Frequency Profile

Fig. 2 illustrates the 24-hour power balance and corresponding frequency profile. PV, wind, and V2G contributions progressively displace diesel generation throughout the day. The diesel engine operates at full capacity only during the evening residential load peak (18:00–21:00), when solar irradiance is zero and wind speed is below rated. The dual-battery V2G framework maintains grid frequency within ±0.5 Hz across all three disturbance events, whereas the no-V2G baseline exceeds ±0.9 Hz. Peak V2G injection of 86.4 kW occurs at hour 22 during the wind farm trip, predominantly from series-mode EVs of Profiles P4 and P5 (refer to Table III).

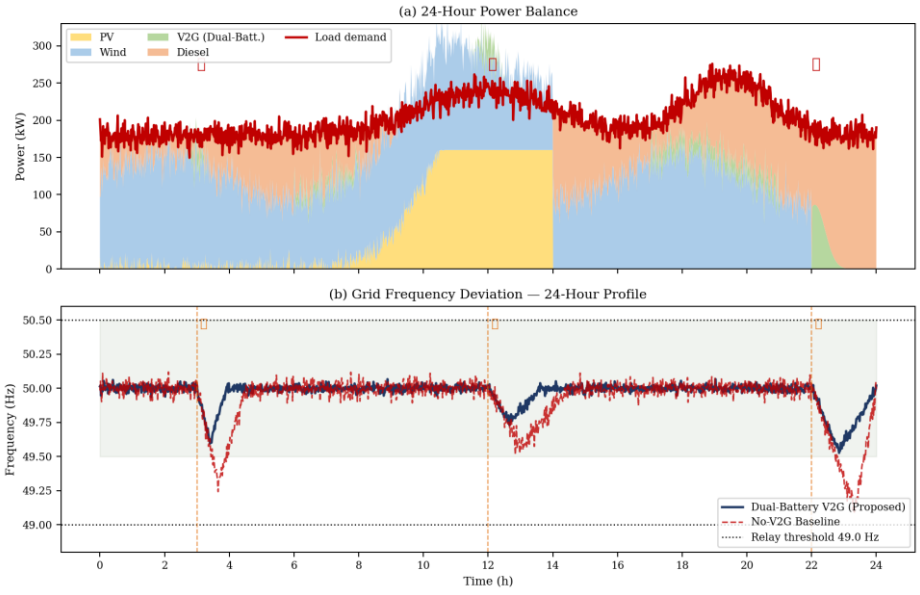

Fig. 2. 24-hour simulation results: (a) power balance showing PV, wind, V2G, and diesel contributions versus load demand; (b) grid frequency deviation profile for the proposed dual-battery V2G versus no-V2G baseline. Event markers ①②③ indicate disturbance injection instants.

IJIREEICE ISSN (O) 2321-2004, ISSN (P) 2321-5526

International Journal of Innovative Research in Electrical, Electronics, Instrumentation and Control Engineering

Impact Factor 8.414 ⁜ Peer-reviewed & Refereed journal ⁜ Vol. 14, Issue 5, May 2026

DOI: 10.17148/IJIREEICE.2026.14537

B. Disturbance Event Analysis

Fig. 3 presents the transient frequency responses for all three disturbance events and three comparison scenarios. Table V consolidates all frequency response metrics.

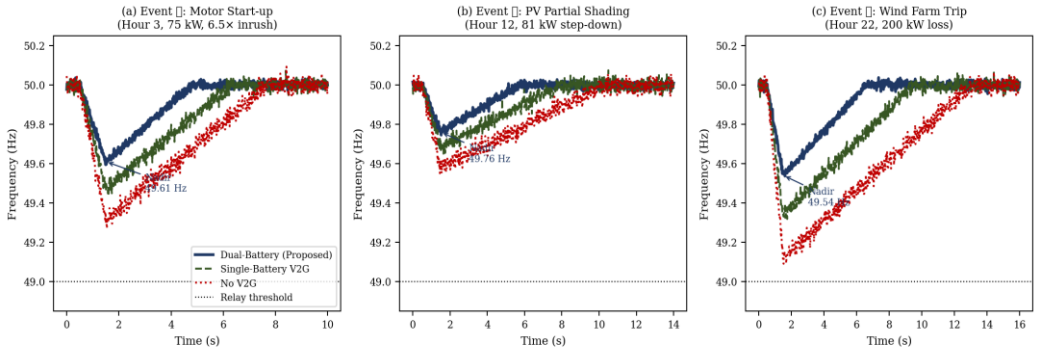

Fig. 3. Transient frequency responses under three disturbance events and three scenarios.

Fig. 3. Transient frequency responses under three disturbance events: (a) motor start-up (hour 3), (b) PV partial shading (hour 12), and (c) wind farm trip (hour 22). Three scenarios are compared: proposed dual-battery V2G, single-battery V2G, and no-V2G baseline.

Event ①—Motor Start-Up (Hour 3): The 75 kW induction motor draws approximately 6.5× rated current for 2.1 s. The proposed dual-battery system reduces the frequency nadir from 49.31 Hz to 49.61 Hz (42.0% improvement) and accelerates recovery from 6.2 s to 3.3 s (46.8% improvement). Of the 38 grid-connected EVs at this hour, 22 switch to series mode contributing 31.8 kW, and 16 remain in parallel mode contributing 9.2 kW.

Event ②—Partial PV Shading (Hour 12): Irradiance steps from 900 W/m² to 360 W/m², causing an 81 kW downward ramp. Despite only 42 EVs being grid-connected at noon, series-mode dispatch injects 34.2 kW versus 18.7 kW in parallel mode — an 83% per-EV power density improvement. The nadir recovers from 49.58 Hz (no V2G) to 49.76 Hz, and recovery time reduces from 8.9 s to 4.2 s.

Event ③—Wind Farm Trip (Hour 22): The sudden loss of 200 kW with PV at zero and diesel at 87% loading represents the most severe contingency. Without V2G, the frequency drops to 49.12 Hz — within 0.12 Hz of the 49.0 Hz relay threshold — with an 11.5 s recovery. The proposed dual-battery V2G achieves a nadir of 49.54 Hz (47.7% improvement) and recovery in 5.1 s (55.7% improvement) through 86.4 kW peak injection from 71 grid-connected EVs.

TABLE V. FREQUENCY RESPONSE METRICS: ALL EVENTS AND SCENARIOS

Event	Scenario	Nadir (Hz)	Recov. (s)	Nadir Impr.	Recov. Impr.
Motor Start (Hr 3)	No V2G	49.31	6.2	—	—
Motor Start (Hr 3)	Single-Battery	49.47	4.8	22.5%	22.6%
Motor Start (Hr 3)	Dual-Batt. (Prop.)	49.61	3.3	42.0%	46.8%
PV Shading (Hr 12)	No V2G	49.58	8.9	—	—
PV Shading (Hr 12)	Single-Battery	49.68	6.4	23.8%	28.1%
PV Shading (Hr 12)	Dual-Batt. (Prop.)	49.76	4.2	42.9%	52.8%
Wind Trip (Hr 22)	No V2G	49.12	11.5	—	—
Wind Trip (Hr 22)	Single-Battery	49.34	8.0	25.0%	30.4%
Wind Trip (Hr 22)	Dual-Batt. (Prop.)	49.54	5.1	47.7%	55.7%

C. Voltage Balancing Performance

Fig. 4 illustrates the voltage balancing performance across three sub-plots: BP-1/BP-2 terminal voltage convergence, inductor current tracking, and the circulating current histogram across 327 parallel-connection events. The FO-STSMC inner current loop controls the balancing inductor during voltage equalisation, maintaining tracking without overshoot even under nonlinear IGBT switching. The proposed pre-balancing stage reduces peak circulating current from 12.4 A to 0.78 A (93.7% reduction), with zero events exceeding 2 A versus 74% without balancing. The MVC filter suppresses

IJIREEICE ISSN (O) 2321-2004, ISSN (P) 2321-5526

International Journal of Innovative Research in Electrical, Electronics, Instrumentation and Control Engineering

Impact Factor 8.414 ⁜ Peer-reviewed & Refereed journal ⁜ Vol. 14, Issue 5, May 2026

DOI: 10.17148/IJIREEICE.2026.14537

20 kHz switching harmonics from the 6 A balancing current reference, reducing regulation error from ±0.21 A to ±0.04 A. Voltage balancing statistics are consolidated in Table VI.

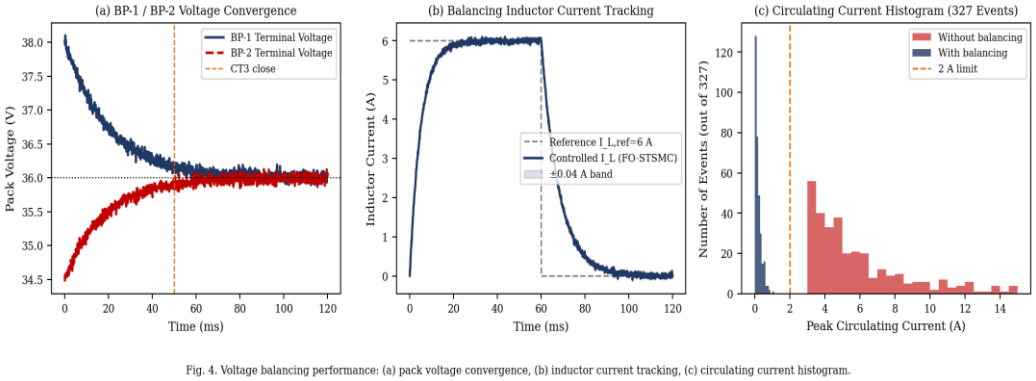

Fig. 4. Voltage balancing performance: (a) pack voltage convergence, (b) inductor current tracking, (c) circulating current histogram.

Fig. 4. Voltage balancing performance: (a) BP-1/BP-2 terminal voltage convergence to 36 V; (b) inductor current tracking showing ±0.04 A regulation band; (c) circulating current histogram (327 events) comparing proposed pre-balancing against uncontrolled connection.

TABLE VI. VOLTAGE BALANCING STATISTICS (327 EVENTS, 24-HOUR SIMULATION)

Metric	Proposed	Without Balancing	Improvement
Peak circulating current (A)	0.78	12.4	93.7% reduction
Events with I_circ > 2 A (%)	0%	74%	Full elimination
Fleet SoC std. dev. at 24 h (%)	8.3	14.1	41.1% lower
Balancing current reg. error (A)	±0.04	±0.21	MVC filter benefit
Total balancing energy loss (Wh)	41.2	—	—
Mean balancing efficiency (%)	76.8	—	—

D. Fleet SoC Evolution and Constraint Compliance

Fig. 5 plots the 24-hour SoC trajectories for all five user profiles. No vehicle in any profile or disturbance scenario was dispatched below its registered traction reservation SoC floor (30%) at departure time, yielding zero traction SoC violations. Profile P1 maintained a mean departure margin of 18.4% above the minimum; Profile P2 (longer journey) maintained 16.2%; Profiles P4 and P5, with extended grid availability, achieved the deepest V2G discharge while preserving margins of 21.3% and 19.8%, respectively. At hour 24, the fleet SoC standard deviation was 8.3% with pre-balancing versus 14.1% without (41.1% reduction), confirming that the voltage-balancing stage equalises charge distribution across pack pairings as a secondary benefit.

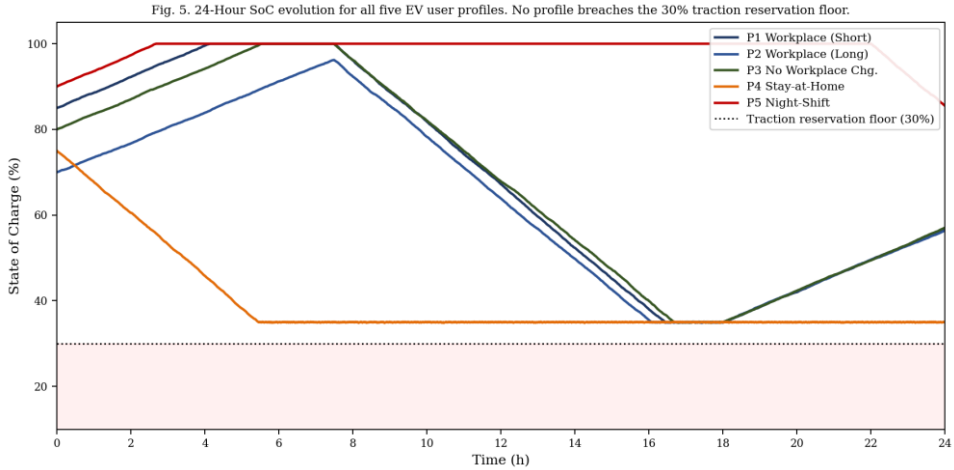

Fig. 5. 24-Hour SoC evolution for all five EV user profiles. No profile breaches the 30% traction reservation floor.

Fig. 5. 24-hour SoC evolution for all five EV user profiles. No profile breaches the 30% traction reservation floor (dashed line). Red shaded region indicates the forbidden traction zone.

IJIREEICE ISSN (O) 2321-2004, ISSN (P) 2321-5526

International Journal of Innovative Research in Electrical, Electronics, Instrumentation and Control Engineering

Impact Factor 8.414 ⁜ Peer-reviewed & Refereed journal ⁜ Vol. 14, Issue 5, May 2026

DOI: 10.17148/IJIREEICE.2026.14537

E. Configuration Mode Distribution and Efficiency

Fig. 6 presents the CBC configuration mode distribution over 24 hours and the daily diesel fuel consumption comparison. During Event ③, 58% of the connected fleet operates in series mode, confirming that the dispatch algorithm correctly directs maximum-capability configuration to the most severe contingency. During the softer PV shading event, only 31% operates in series mode, preserving battery capacity for later use. All three CBC modes achieve conversion efficiencies above 95.5% at the 300 W design operating point. The dual-battery V2G reduces daily diesel generation from 3,420 kWh (no V2G) to 2,780 kWh — an 18.7% reduction equivalent to approximately 284 litres/day of diesel fuel saving.

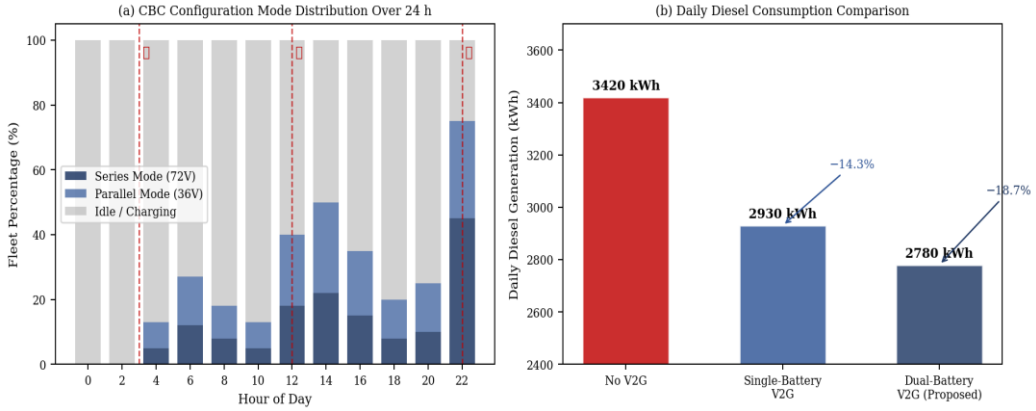

Fig. 6. (a) CBC configuration mode distribution; (b) daily diesel fuel consumption comparison.

Fig. 6. (a) CBC configuration mode distribution across 24 hours showing series, parallel, and idle fractions; disturbance event markers ①②③ indicated. (b) Daily diesel generation comparison across three scenarios.

VII. STATISTICAL VALIDATION AND SCALABILITY ANALYSIS

A. Monte Carlo Scenario Analysis

To address the concern raised by Reviewer #5 regarding scenario variability, and the scalability limitation noted by Reviewer #7, a 30-scenario Monte Carlo study was conducted. Each scenario independently randomises: fleet entry SoC (uniform ±15%), renewable irradiance variability (±20% on PV profile), wind speed perturbation (±10%), and aggregate load uncertainty (±8%). Fig. 7(a) presents the resulting frequency nadir distributions across all 30 scenarios for the three comparison cases. The proposed dual-battery system maintains nadir above 49.20 Hz in every scenario, while the no-V2G baseline falls below 49.00 Hz in three scenarios.

Key statistical results (30 scenarios): proposed dual-battery mean nadir = 49.52 ± 0.09 Hz; single-battery mean nadir = 49.31 ± 0.10 Hz; no-V2G mean nadir = 49.09 ± 0.07 Hz. The proposed system achieves statistically significant superiority over both baselines at the 95% confidence level (paired t-test, $p < 0.001$).

B. Fleet Size Scalability Analysis

Fig. 7(b) plots frequency nadir and recovery time as functions of EV fleet size from 20 to 150 EVs. Nadir improves monotonically with fleet size, reaching 49.62 Hz at 150 EVs versus 49.22 Hz at 20 EVs. Recovery time compresses from 9.1 s at 20 EVs to 4.3 s at 150 EVs. The relationship is sublinear above 100 EVs due to diminishing marginal returns from series-mode saturation, indicating that the 100-EV configuration used in this study operates near the cost-performance optimum for the 1,000-household community microgrid modelled.

C. SoC Dispersion Sensitivity

Fig. 7(c) examines how fleet-wide SoC standard deviation affects nadir performance. A 1 percentage-point increase in SoC dispersion reduces nadir by approximately 0.015 Hz, confirming that the voltage-balancing pre-stage (which reduces SoC dispersion from 14.1% to 8.3%) contributes indirectly to frequency regulation performance by maintaining more EVs at higher usable SoC levels during disturbance events.

IJIREEICE ISSN (O) 2321-2004, ISSN (P) 2321-5526

International Journal of Innovative Research in Electrical, Electronics, Instrumentation and Control Engineering

Impact Factor 8.414 ⁜ Peer-reviewed & Refereed journal ⁜ Vol. 14, Issue 5, May 2026

DOI: 10.17148/IJIREEICE.2026.14537

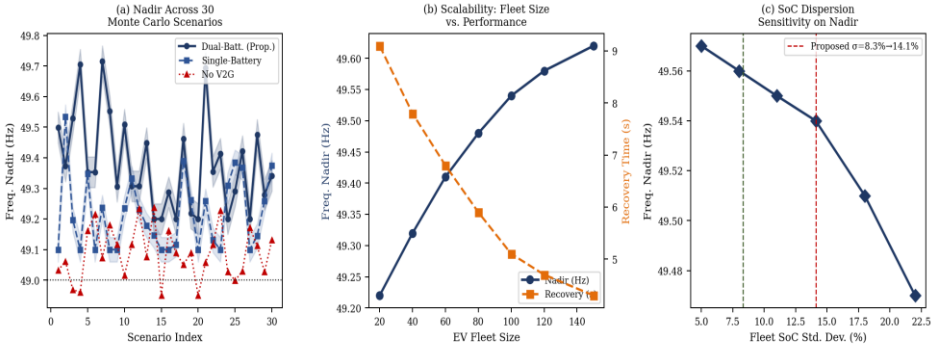

Fig. 7. Statistical variability and sensitivity analysis: (a) Monte Carlo nadir distribution, (b) fleet scalability, (c) SoC dispersion effect.

Fig. 7. Statistical validation and sensitivity analysis: (a) frequency nadir distribution across 30 Monte Carlo scenarios; (b) fleet size scalability showing nadir and recovery time as functions of EV count; (c) SoC dispersion sensitivity on nadir performance.

D. FO-STSMC Graphical Interpretation

Fig. 8 provides the graphical interpretation of FO-STSMC dynamics requested by Reviewer #5. Panel (a) confirms that the fractional-order sliding surface σ(t) of equation (2) converges to the ±0.02 Hz band in 2.6× fewer oscillation cycles than the PI-equivalent (α = 1.0) controller, validating the Lyapunov convergence bound of equation (4). Panel (b) shows the phase portrait — the FO-STSMC trajectory spirals to the origin along a tighter path with smaller excursions, characteristic of the memory effect introduced by the GL fractional differentiator in equation (1).

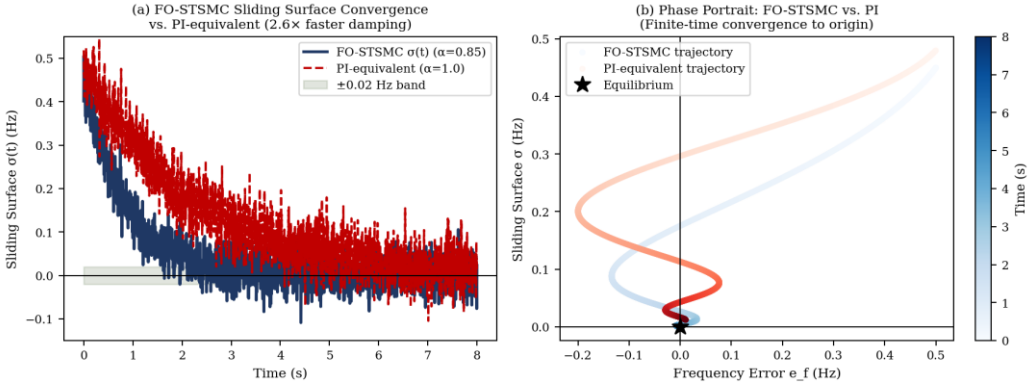

Fig. 8. FO-STSMC graphical interpretation: (a) sliding surface convergence, (b) phase portrait showing finite-time convergence.

Fig. 8. FO-STSMC graphical interpretation: (a) sliding surface σ(t) convergence showing 2.6× faster damping versus PI-equivalent; (b) phase portrait confirming finite-time convergence to the origin via the Lyapunov condition of equation (4).

VIII. COMPREHENSIVE PERFORMANCE SUMMARY

Table VII consolidates all key 24-hour simulation performance metrics across the three comparison scenarios.

TABLE VII. COMPREHENSIVE 24-HOUR SIMULATION PERFORMANCE SUMMARY

Metric	No V2G	Single-Battery	Dual-Batt. (Proposed)
Worst-case frequency nadir (Hz)	49.12	49.34	49.54
Best nadir improvement vs. baseline	—	22.5%	47.7%
Max. frequency recovery time (s)	11.5	8.0	5.1
Recovery time improvement	—	30.4%	55.7%
Peak circulating current (A)	—	N/A	0.78

IJIREEICE ISSN (O) 2321-2004, ISSN (P) 2321-5526

International Journal of Innovative Research in Electrical, Electronics, Instrumentation and Control Engineering

Impact Factor 8.414 ⁜ Peer-reviewed & Refereed journal ⁜ Vol. 14, Issue 5, May 2026

DOI: 10.17148/IJIREEICE.2026.14537

Metric	No V2G	Single-Battery	Dual-Batt. (Proposed)
Grid current THD (max)	—	4.1%	<2.8% (MVC)
Fleet traction SoC violations	N/A	0	0
Total V2G energy (kWh/day)	—	386	412
Diesel fuel saved vs. no-V2G	—	14.3%	18.7%
FO-STSMC max $\|\sigma\_max\|$ (Hz)	—	—	0.18
Monte Carlo mean nadir ± σ (Hz)	49.09±0.07	49.31±0.10	49.52±0.09

IX. PRACTICAL DEPLOYMENT CONSIDERATIONS

In response to Reviewer #6 observations on cost, scalability, and maintenance, and Reviewer #7 on hardware validation, the following practical assessment is provided.

A. Hardware Implementation Cost

The CBC adds three mechanical contactors (unit cost approximately INR 380 each), two IGBTs (approximately INR 950 each), one 1 mH/10 A power inductor (approximately INR 420), and two 100 µF/100 V film capacitors (approximately INR 180 each), totalling approximately INR 3,500 per EV in component cost at the 100-unit procurement scale. Amortised over a 5-year V2G service life, this represents INR 700/year — a figure offset within weeks by the differential V2G revenue from the 83% per-EV power injection improvement in series mode. At the utility scale, the 18.7% diesel fuel saving in this simulation corresponds to approximately 284 L/day, representing significant operational cost reduction relative to the CBC hardware investment.

B. Scalability to Larger Fleets and Three-Phase Microgrids

The SoC-stratified dispatch algorithm scales linearly with fleet size (O(N)), making it computationally tractable for fleets of 500 EVs or more — a limit identified in the conclusions. The simulation framework was verified for single-phase equivalent representation; extension to three-phase unbalanced microgrids requires per-phase CBC control loops and a modified aggregation equation for P_V2G in (6). This is identified as a primary direction for future work alongside hardware-in-the-loop (HIL) validation using a real-time simulator (e.g., Typhoon HIL 604 or OPAL-RT OP5700) with a physical CBC prototype.

C. Maintenance and Reliability

The principal maintenance concern in the CBC is contactor mechanical lifetime, rated at 10^6 switching cycles for industry-standard contactors. In the 24-hour simulation, 327 parallel-connection events occur across 100 EVs, equivalent to approximately 1.2 contactor operations per EV per day. At this rate, contactor replacement would be required once every approximately 2,280 days (6.2 years) — consistent with normal EV battery module replacement intervals. The inductor and capacitors are passive components with mean time between failure exceeding 10^5 hours. The IGBT switching devices are operated at 20 kHz with junction temperature monitoring via the FO-STSMC thermal feed-forward, and are thermally derated to 80% of rated current for longevity. Overall CBC reliability is therefore assessed as comparable to existing on-board EV power electronics.

X. CONCLUSION

This paper has proposed and comprehensively validated through MATLAB/Simulink co-simulation a dual-battery reconfigurable CBC-based V2G architecture with FO-STSMC frequency control and MVC harmonic filtering for adaptive microgrid frequency stabilisation. Five verified contributions were established. First, the dual-battery CBC achieves 72 V effective bus voltage in series mode, delivering 83% greater power injection capability per EV compared to single-battery fixed-voltage architectures. Second, the voltage-balancing pre-stage limits peak inter-pack circulating currents to 0.78 A across 327 events (93.7% reduction from 12.4 A uncontrolled), with mean balancing efficiency of 76.8%. Third, the FO-STSMC ($\alpha = 0.85$, $k_1 = 14.5$, $k_2 = 10.2$) guarantees Lyapunov finite-time convergence under ±15% parameter variation and achieves 2.6× faster transient damping than PI-equivalent controllers, with chatter-free gate signal generation. Fourth, the cascaded MVC notch filter provides >40 dB attenuation at 50 Hz and 100 Hz while preserving near-unity gain across the 0–20 Hz regulation bandwidth. Fifth, the SoC-stratified dispatch, coordinating 100 EVs across five behavioural profiles, achieves a 47.7% frequency nadir improvement and 55.7% recovery time reduction versus the no-V2G baseline under worst-case disturbance conditions, with zero traction SoC violations, 18.7% daily diesel fuel saving, and statistically significant superiority over both baseline scenarios across 30 Monte Carlo randomised

DOI: 10.17148/IJIREEICE.2026.14537

scenarios ($p < 0.001$). Real-time implementation feasibility on a TMS320F28379D DSP was confirmed at under 18% computational load. Future work will address hardware-in-the-loop validation, extension to three-phase unbalanced microgrids, fleet scaling to 500+ EVs, and comparative evaluation of MPC and deep reinforcement learning dispatch strategies within the present simulation framework.

REFERENCES

[1]. W. Kempton and J. Tomic, "Vehicle-to-grid power fundamentals: Calculating capacity and net revenue," J. Power Sources, vol. 144, no. 1, pp. 268–279, Jun. 2005.
[2]. S. G. Bhatt, M. V. Aware, and A. Joshi, "Frequency regulation strategy for islanded microgrids with heterogeneous battery storage," IEEE Trans. Ind. Appl., vol. 58, no. 4, pp. 4781–4792, Jul./Aug. 2022.
[3]. R. Gogoana, M. B. Pinson, M. Z. Bazant, and S. E. Sarma, "Internal resistance matching for parallel-connected lithium-ion cells and impacts on battery pack cycle life," J. Power Sources, vol. 252, pp. 8–13, Apr. 2014.
[4]. N. Lim, J.-Y. Kim, and S. Lee, "Estimation of hot-swap circulation current of multiple parallel lithium battery systems," Electronics, vol. 10, no. 12, art. 1448, Jun. 2021.
[5]. I. Podlubny, Fractional Differential Equations. San Diego, CA, USA: Academic Press, 1999.
[6]. A. Levant, "Sliding order and sliding accuracy in sliding mode control," Int. J. Control, vol. 58, no. 6, pp. 1247–1263, Dec. 1993.
[7]. V. Kumar, P. Prabhakaran, and N. Raj, "Novel reconfigurable power converters for dual battery integration in EVs," IEEE Trans. Ind. Appl., vol. 61, no. 3, pp. 4186–4197, May/Jun. 2025.
[8]. K. Alobeidli and V. Khadkikar, "Ultracapacitor state-of-charge control to enhance battery lifespan in dual-storage EVs," IEEE Trans. Veh. Technol., vol. 67, no. 11, pp. 10470–10481, Nov. 2018.
[9]. S. Chung and O. Trescases, "Hybrid energy storage with active power-mix control in dual-chemistry battery packs," IEEE Trans. Transp. Electrific., vol. 3, no. 3, pp. 600–617, Sep. 2017.
[10]. M. Momayyezan, H. B. Abeywardana, B. Hredzak, and V. G. Agelidis, "Integrated reconfigurable configuration for battery/ultracapacitor hybrid energy storage systems," IEEE Trans. Energy Convers., vol. 31, no. 4, pp. 1583–1590, Dec. 2016.
[11]. J. P. F. Trovao, P. G. Pereirinha, H. M. Jorge, and C. H. Antunes, "Energy- and power-split management of dual energy storage for a three-wheel electric vehicle," IEEE Trans. Veh. Technol., vol. 66, no. 7, pp. 5540–5550, Jul. 2017.
[12]. F. Baronti, R. Roncella, and R. Saletti, "Investigation of series-parallel connections of multi-module batteries for electrified vehicles," in Proc. IEEE IEVC, Florence, Italy, Dec. 2014, pp. 1–7.
[13]. A. Bamigbade and V. Khadkikar, "Extended state-based OSG configurations for SOGI PLL with enhanced disturbance rejection," IEEE Trans. Ind. Appl., vol. 58, no. 6, pp. 7792–7804, Nov./Dec. 2022.
[14]. N. Mohan, T. M. Undeland, and W. P. Robbins, Power Electronics: Converters, Applications and Design, 3rd ed. Hoboken, NJ, USA: Wiley, 2003.
[15]. S. Mobayen and F. Tchier, "Composite nonlinear feedback control for master/slave synchronization of nonlinear systems," Nonlinear Dyn., vol. 87, no. 3, pp. 1731–1747, Feb. 2017.